

The Diurnal Cycle of Cloud-Top Height and Cloud Cover over the Southeastern Pacific as Observed by *GOES-10*

DAVID PAINEMAL AND PATRICK MINNIS

NASA Langley Research Center, Hampton, Virginia

LARRY O'NEILL

College of Earth and Atmospheric Sciences, Oregon State University, Corvallis, Oregon

(Manuscript received 26 November 2012, in final form 14 March 2013)

ABSTRACT

The diurnal cycles in cloud-top height H_{top} and cloud fraction (CF) in the southeastern Pacific stratocumulus region were determined for October–November 2008 by analyzing data from *Geostationary Operational Environmental Satellite-10 (GOES-10)* according to a diurnal/semidiurnal harmonic fitting technique. The value of H_{top} was obtained by applying a formula based on a linear regression of the differences between *GOES-10* cloud-top temperature and Tropical Rainfall Measuring Mission (TRMM) Microwave Imager (TMI) satellite sea surface temperature, with a common $0.25^\circ \times 0.25^\circ$ spatial resolution. A satellite liquid water path (LWP) climatology complemented this dataset.

Southwestward transects of H_{top} and LWP anomalies reveal a coherent propagating signal from the coast in the afternoon, with a typical phase speed of 25 m s^{-1} . This pattern is preceded by a subsidence wave that reaches its peak a few hours before the maximum in H_{top} and LWP anomalies. Coincident increases in LWP and H_{top} after the subsidence wave passes suggest that the boundary layer deepening promotes cloud thickening and increased LWP, which are likely maintained through a well-mixed boundary layer and sufficient moisture fluxes that can counteract the effect of dry air entrainment. The interference between the radiatively and subsidence wave–driven cycles gives rise to a semidiurnal cycle in H_{top} along the coast. While the semidiurnal amplitude is near 80 m close to the coast with a fraction of explained variance greater than 0.4, it decreases to 30 m offshore (80°W). Similar to H_{top} , CF also exhibits contrasting zonal differences, but with a smaller semidiurnal component. The phase of the semidiurnal harmonic resembles the subsidence propagation westward, and the noticeable land–sea breeze circulation at 26°S that extends 200 km offshore.

1. Introduction

The variability in marine stratocumulus clouds is strongly linked to the processes that govern the evolution of the boundary layer. Entrainment, subsidence, advection, and turbulent fluxes determine changes in both cloud properties and boundary layer depth. Over diurnal time scales, the modulation of the different dynamical processes is manifested in a distinct cycle in cloud-top height and cloud cover (e.g., Minnis et al. 1992, hereafter M92; Zuidema et al. 2009, hereafter Z09). While different observational studies report similar diurnal cycles over different marine stratocumulus regions,

that is, a boundary layer deepening (cloud-cover increase) during the early morning and shoaling (cloud-cover decrease) in the afternoon (Wood 2012, and references therein), the amplitudes and phases are unique over the southeastern Pacific (e.g., Minnis and Harrison 1984; Z09). This poses a challenge for numerical models, which systematically underestimate the boundary layer depth and misrepresent the cloud fraction and liquid water path (LWP) cycle in this region (e.g., Wyant et al. 2010; Abel et al. 2010).

The unique features of the southeastern Pacific boundary layer are attributed to modulation by the Andes cordillera, situated at the eastern boundary of the cloud regime, which reaches altitudes up to 5 km along the western coast of South America (e.g., Xu et al. 2004; Richter and Mechoso 2006). Minnis and Harrison (1984) suggested that continental-scale convection over the

Corresponding author address: Dr. David Painemal, NASA Langley Research Center, Hampton, VA 23681.
E-mail: david.painemal@nasa.gov

Amazon basin drives a diurnal pulse in the surrounding subsidence fields resulting in the deep and complex diurnal cycle in the southeastern Pacific marine stratocumulus. However, analyses of numerical simulations indicate that the daily afternoon heating of the cordillera's western slope and associated dry convection induces a circulation that triggers anomalous upward motions in the lower troposphere, with a perturbation that propagates southwestward as a gravity wave at speeds of around $25\text{--}34\text{ m s}^{-1}$ [30 m s^{-1} in Garreaud and Muñoz (2004), $25\text{--}34\text{ m s}^{-1}$ in Rahn and Garreaud (2010), and 25 m s^{-1} in Toniazzo et al. (2011) and Wood et al. (2009)]. Diurnal subsidence modulation in the evolution of the marine boundary layer depth is suggested in satellite observations of cloud-top height (Z09). Moreover, variations in the cloud water content due to the subsidence cycle are plausible, as the latter exerts control over the cloud-top mixing (entrainment) and the boundary layer turbulence. In this regard, a relationship between subsidence and satellite microwave liquid water path is evinced over the southeastern Pacific (Wood et al. 2009). Specifically, a southwestward-propagating liquid water path signal occurs in concert with a propagating subsidence pattern, with liquid water path anomalies that peak a few hours after the maximum in anomalous upward motion (Wood et al. 2009). It is also likely that the subsidence forcing is the cause for the semidiurnal-cycle occurrence in liquid water path near the Chile–Peru coast (O'Dell et al. 2008). Although the semidiurnal cycle in cloud-top height was also documented over this region with in situ observations (e.g., de Szoeke et al. 2012), sampling limitations prevented a detailed description of the extent of the subsidence modulation, and the nuances of the boundary layer depth variability are unknown. While other gravity wave perturbations, like that originated from the subtropical jet stream, can also dramatically alter the cloud properties at synoptic scales (Allen et al. 2012), the Andes-driven subsidence wave has a first-order climate impact in the southeastern Pacific boundary layer evolution at diurnal and seasonal scales (Garreaud and Muñoz 2004).

The proper quantitative evaluation of the boundary layer height evolution is fundamental to understanding the processes that drive its variability. An accurate description of the diurnal cycle is also valuable for model validation, especially over the southeastern Pacific, the location of one of the most extended and persistent stratocumulus cloud regimes on the planet, where numerical models fail to produce realistic marine boundary layer depths (Wyant et al. 2010).

In this study we use satellite retrievals from *Geostationary Operational Environmental Satellite-10* (*GOES-10*) imager radiances to document the diurnal cycle of the

boundary layer depth over the southeastern Pacific during the October–November 2008 time period. Similar to M92 and Z09, we rely on a linear relationship between surface–cloud-top temperature differences and the cloud-top height to determine cloud-top height using retrievals of cloud-top temperature from *GOES-10*. This technique is preferred to other passive-based cloud-top-height algorithms, like that used to analyze Moderate Resolution Imaging Spectroradiometer (MODIS) data (Menzel et al. 2008), that are well known for systematically overestimating the actual cloud-top height over regions with a strong temperature inversion (e.g., Holz et al. 2008; Garay et al. 2008). While other active-based cloud-top retrievals might be more accurate than the linear regression presented here, such as those from satellite-borne lidar *Cloud–Aerosol Lidar and Infrared Pathfinder Satellite Observations* (*CALIPSO*) and GPS radio occultation measurements, their spatial and temporal resolution are limited and inadequate for the investigation of the diurnal cycle [see discussions in Z09 and Xie et al. (2012)].

An objective of this paper is to extend the work by Z09, which relied on four daily MODIS scans, by fully resolving the diurnal cycle in boundary layer depth and cloud fraction. In addition, our analysis follows and expands on the pioneering work of Minnis and Harrison (1984) on the use of GOES retrievals to study the diurnal cycles of cloud fractions and cloud temperature over the southeastern Pacific. Here we analyze 2 months of data and evaluate the results in the context of the observations collected during the Variability of the American Monsoon System (VAMOS)–Ocean–Cloud–Atmosphere–Land Study (VOCALS) Regional Experiment (VOCALS-REX; Wood et al. 2011) and other VOCALS-related observations. Our main focus is on the link between boundary layer variability, cloud properties, and the mesoscale circulation that is driven by the Andes cordillera.

This work complements our previous validation assessment of *GOES-10* cloud microphysical property retrievals, which also includes the investigation of the microphysical daytime cycle over the same region of study (Painemal et al. 2012). The implications of this work and Painemal et al. (2012) will be also discussed.

2. Dataset

a. Satellite retrievals

Cloud-top temperature and cloudy-scene identification were determined for this study from the *GOES-10* radiances using algorithms adapted from MODIS observations for the Clouds and Earth's Radiant Energy

System (CERES) edition 2 Single Scanner Footprint (SSF; Minnis et al. 2011). The *GOES-10* radiances are taken at a nominal resolution of approximately 4 km, with retrievals produced every 30 min. Specifically, the algorithm for retrieving cloud-top temperature is strongly dependent on the $10.7\text{-}\mu\text{m}$ radiance and cloud emittance, which is in turn a function of the cloud optical depth (Minnis et al. 2011). The algorithm also accounts for atmospheric absorption of water vapor and other gases. The identification of cloudy pixels follows the cascading threshold algorithm described in Minnis et al. (2008), which is applied to four (three during nighttime) *GOES-10* channels. As in Painemal et al. (2012), unless otherwise noted, we average the cloud-top temperature T_{top} retrievals to a 0.25° resolution. In addition, we define the cloud fraction (CF) as the ratio between the number of cloudy pixels and the total number of pixels within the $0.25^\circ \times 0.25^\circ$ grid. Finally, we limit our analysis to pixels and grids having $T_{\text{top}} > 0^\circ\text{C}$ and $\text{CF} > 0.9$.

Because the cloud-top-height algorithm is based on the temperature differences between cloud top and sea surface, we utilize 3-day-mean sea surface temperature (SST) maps from the Tropical Rainfall Measurement Mission (TRMM) Microwave Imager (TMI) (SST_{TMI}) at a 0.25° spatial resolution (Wentz et al. 2000). Given the TRMM's narrower field of view than that from *GOES-10*, the use of a 3-day mean provides the appropriate spatial coverage to be combined with *GOES-10* retrievals. One of the main advantages of TMI is its ability to measure SST in the presence of clouds, aerosols, and atmospheric water vapor, which is particularly important in the southeastern Pacific given the persistent stratocumulus cloud deck. Through comparisons with bulk buoy SSTs near the equator, Gentemann et al. (2004) estimated accuracies of individual TMI SST measurements of 0.57°C . The diurnal cycle of SST during October and November in the southeastern Pacific has been shown to be less than 0.3°C (e.g., Fig. 5 in Kawai and Wada 2007), whereas its *GOES-10* T_{top} counterpart reached amplitudes up to 3°C during VOCALS-REx. Given the negligible diurnal cycle in SST compared to that for T_{top} and the small day-to-day sea surface temperature variability, the use of 3-day-mean maps is a small source of error.

Additionally, we further complement the analysis with an LWP climatology for the October–November 2002–09 period. Estimates of the LWP diurnal cycle were obtained from four passive microwave radiometers: the TMI, the Advanced Microwave Scanning Radiometer for Earth Observing System (EOS) (AMSR-E) for the *Aqua* satellite, and the Special Sensor Microwave Imager (SSM/I) *FI3* and *FI5* satellites. These estimates were produced and

distributed by Remote Sensing Systems (RSS). The RSS datasets used for these analyses are version 6 for the SSM/I *FI3* and *FI5*, version 4 for TMI, and version 5 for AMSR-E. The LWP estimates are gridded onto a uniform $0.25^\circ \times 0.25^\circ$ latitude–longitude spatial grid separately for each ascending and descending orbit. With this four-satellite combination, each 0.25° grid cell is sampled approximately 140–200 times per month in the southeastern Pacific, or about 4–7 times per day (O'Neill et al. 2011), which is adequate to resolve diurnal and semidiurnal LWP variability. Further descriptions of the development of the LWP diurnal and semidiurnal cycle climatology over the southeastern Pacific are in O'Neill et al. (2011). The accuracy of individual LWP estimates from these passive microwave radiometers has been estimated at 25 g m^{-2} (Wentz 1997; Wentz and Meissner 2000). While uncertainties in passive microwave estimates of LWP can occur from precipitation and relatively large frozen water particles [see the summary in O'Dell et al. (2008)], neither is significant in the southeastern Pacific as precipitation is generally light and frozen water is infrequent.

b. *In situ* observations

In situ cloud-top temperature and height are used to establish the linear relationship that is subsequently applied to the satellite observations. *In situ* cloud-top temperatures and heights were collected in nearly 80 vertical profiles conducted by the C-130 research aircraft during 1 month of VOCALS-REx operations (15 October–15 November 2008). Vertical profiles were performed between 0100 and 1700 local solar time (LST), at different locations, with an approximate vertical resolution of 5–6 m. The cloud top is defined as the highest point of the cloud vertical profile in which the liquid water content (from a hot-wire probe) was larger than 0.04 g m^{-3} (e.g., Wood et al. 2011; Painemal and Zuidema 2011). Given the sensitivity of standard temperature probes to the liquid water, we used radiometric-based temperatures from the fast-response Ophir-III ($4.25\text{-}\mu\text{m}$ wavelength). Ophir-III performed well during the flights and compared well with other probes (more information available at: http://data.eol.ucar.edu/master_list/?project=VOCALS).

3. *GOES-10* temperature assessment

We first compared collocated *GOES-10*- and CERES-MODIS-based T_{top} values that were retrieved using the algorithm for CERES SSF, edition 2, as described in section 2. The CERES-MODIS T_{top} is produced at the CERES footprint resolution ($\sim 20\text{ km}$) as averages computed from subsampled 1-km cloud microphysical retrievals, using convolution with the CERES scanner

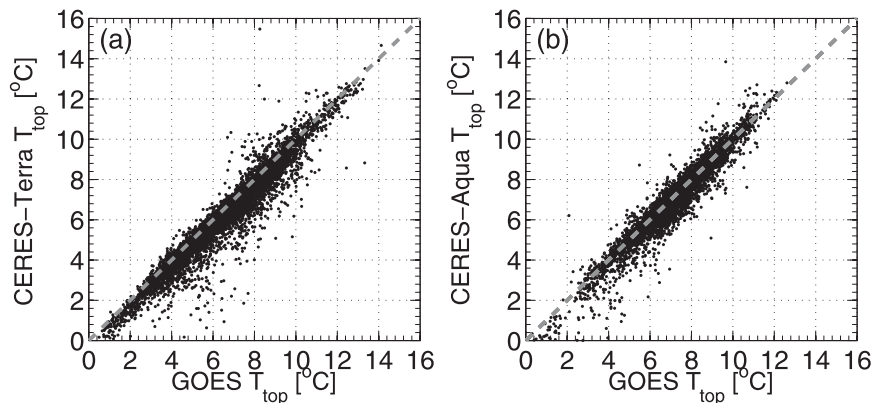


FIG. 1. Comparison of daytime GOES T_{top} and CERES-MODIS-based T_{top} from (a) *Terra* and (b) *Aqua*.

point spread function. The comparison between *GOES-10* and CERES-MODIS is valuable given the better-characterized radiometric response of MODIS instrument. CERES-MODIS retrievals from *Terra* and *Aqua* were collocated within ± 20 min of the 1530 and 1945 UTC *GOES-10* scans, respectively. As noted in Painemal and Minnis (2012), in order to produce uniformly gridded fields, the retrievals were averaged to a common 0.5° resolution because the CERES SSF product is collocated with the CERES footprint and is therefore irregularly sampled. Additionally, the comparison was limited to grids with $\text{CF} > 0.9$.

Temperature scatterplots in Fig. 1 show high correlations ($r \sim 0.96$) and small positive biases of 0.29° and 0.1°C in T_{top} (*GOES-10*) relative to retrievals from the morning (*Terra*) and afternoon (*Aqua*) MODIS overpasses, respectively. The root-mean-square (RMS) differences are less than 0.57°C . This demonstrates the overall good calibration of the *GOES-10* infrared-window channel relative to its MODIS counterpart.

For a second assessment, we compared T_{top} (*GOES-10*) against in situ aircraft measurements collected during the VOCALS-REx field campaign, following the same procedure as in Painemal et al. (2012). That is, the satellite retrievals were regridded to a 20-km resolution and the satellite scan was taken within ± 18 min of the vertical profile occurrence. The comparison was restricted to cloudy scenes, determined from both aircraft and satellite observations. The satellite and in situ T_{top} values (Fig. 2) are well correlated ($r = 0.86$), but with a negative T_{top} (*GOES-10*) offset of 0.96°C and an RMS error of 1.5°C . Using *GOES-8* retrievals and ship-based soundings, Garreaud et al. (2001) found similar differences in the satellite cloud-top and inversion-base temperatures. A similar negative bias, -1.3°C , was found by Z09 using T_{top} from the MODIS Science Team (Menzel

et al. 2008) and an independent in situ dataset. The slightly colder bias for MODIS T_{top} in Z09 is consistent with the tendency of MODIS collection 5 retrievals to remove pixels near the cloud edges or optically thin cloudy pixels. Given the warmer ocean temperature relative to that at the cloud top, the thermal ocean contribution in semitransparent or broken clouds scenes would produce slightly warmer *GOES-10* T_{top} values than their MODIS counterparts.

The negative satellite in situ T_{top} offset here, statistically significant at a 99% confidence level according to the Student's t test, is inconsistent with most of the identified sources of uncertainty. Uncertainties associated with the retrieval algorithm would only account for a modest error in T_{top} . The uncertainty in the cloud-emissivity approximation would yield an error near 0.06°C (Minnis et al. 1998). Additionally, as explained

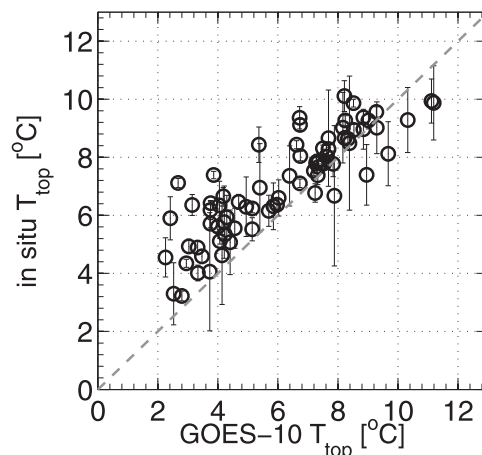


FIG. 2. Scatterplot between collocated *GOES-10* T_{top} and in situ T_{top} . Error bars denote the *GOES-10* standard deviation over a 20-km area.

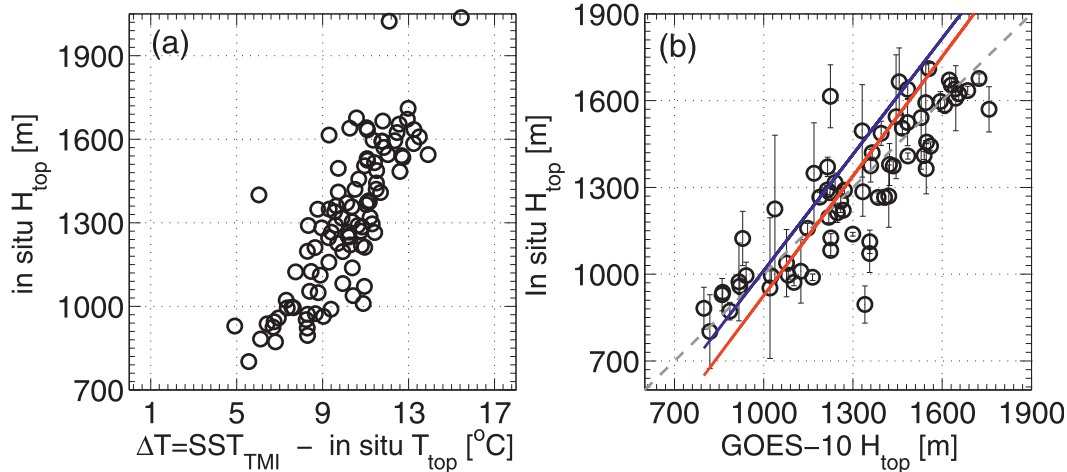


FIG. 3. Temperature and height comparisons. (a) $\Delta T = \text{SST}_{\text{TMI}} - T_{\text{top}}$ (in situ) vs H_{top} (in situ). (b) H_{top} (GOES-10) from Eq. (2) vs in situ H_{top} . Error bars denote the GOES-10 standard deviation over a 20-km area. Red and blue lines denote H_{top} derived using the relationships in Z09 and M92, respectively.

previously, if any error could be attributed to the effect of some thin or broken clouds, this would be a warming, rather than a cooling, impact. For optically thick clouds (optical depth greater than 6), the effective radiating temperature corresponds to an altitude equivalent to an optical depth of about 1.1 (Minnis et al. 2008). For a stratus cloud, this would be roughly 50 m below the actual cloud top. Because the cloud/air temperature monotonically decreases with height, with the coldest temperature at the cloud top, the radiating temperature retrieved from the observations would result in a slight warm bias. Concerning the aircraft instrumentation, potential artifacts in the Ophir-III measurements are discounted as a source for the offset, since similar results were obtained with other aircraft temperature probes. One possible cause of the discrepancy, systematic underestimates of the atmospheric water vapor above the cloud, could account for some of the difference. Keeping in mind that both GOES-10 (CERES) and MODIS T_{top} were found to be cooler than the in situ T_{top} , the water vapor hypothesis would require that the above-cloud humidity is significantly biased in two different numerical weather analyses since the CERES (Minnis et al. 2011) and MODIS team (Menzel et al. 2008) algorithms use different products.

Two other processes may contribute to the temperature discrepancies. Because entrainment and evaporation occur at cloud top, the droplets could be colder than the ambient air. In addition, cloud-top longwave radiative cooling might work in concert to yield drops slightly colder than the air temperature. Thus, because the satellite retrievals primarily measure emission from the clouds, they would yield a lower temperature than

that of the ambient air as well. This implies that the satellite bias should be larger during the night and early morning, when the radiative cooling and entrainment are the strongest (e.g., Caldwell and Bretherton 2009). Interestingly, we found GOES-10 biases of -1.3° and -0.56°C for measurements collected before and after 0800 local time, respectively. Although the diurnal variation of the temperature bias seems to point to the droplet cooling effect, this hypothesis will require further inspection beyond the scope of this study.

Cloud-top-height calculation

Figure 3 depicts the relationship between the temperature difference, $\Delta T = \text{SST}_{\text{TMI}} - T_{\text{top}}$ (in situ) and cloud-top height H_{top} , where SST_{TMI} was interpolated to the vertical profile location. The correlation between ΔT and H_{top} was high ($r = 0.8$), with only a couple of points departing from the trend. This relationship, expressed in Eq. (1), demonstrates that a simple linear fit is a suitable approach to determine H_{top} from ΔT :

$$H_{\text{top}} = \frac{\Delta T + 2.3}{0.0095} [\text{m}]. \quad (1)$$

Before applying the linear regression in Eq. (1) to the satellite observations, we first account for the negative GOES-10 temperature bias by adding 0.95°C to GOES-10, that is,

$$H_{\text{top}} = \frac{\Delta T + 1.35}{0.0095} [\text{m}], \quad (2)$$

with $\Delta T = \text{SST}_{\text{TMI}} - T_{\text{top}}$ (GOES-10).

We applied Eq. (2) to *GOES-10* cloudy scenes ($CF > 0.9$) and compared collocated satellite and in situ H_{top} values (Fig. 3b). We found a correlation of 0.86, a mean bias of 5.4 m, and an RMS error of 135 m, values that demonstrate the goodness of the linear fit. As a comparison, we also included the slope between Eq. (2) (abscissa) and H_{top} estimated using the constant lapse rate of 7.1 K km^{-1} in M92 and the method in Z09 (blue and red lines, respectively, in Fig. 3). Qualitatively, both M92 and Z09 yield similar cloud-top-height estimates, implying good correlations with the in situ cloud-top-height measurements. Nevertheless, M92 (blue line) tends to overestimate the heights at a rate that increases with H_{top} . In contrast, Z09 produces underestimates for small H_{top} , transitioning to magnitudes close to the current fit for heights between 1000 and 1300 m, and overestimates at higher altitudes.

We note here that no inferences were made about the temperature lapse rate $\Gamma = \Delta T/H_{top}$ and H_{top} , as in Z09, given their lack of correlation ($r < 0.4$). Thus, our practical approach simply minimizes the errors in the estimates relative to the in situ H_{top} . Because Eq. (2) is empirical, error sensitivity tests are difficult. The errors depend on the linearity of the ΔT and H_{top} relationship and the inherent biases in the satellite retrievals. Nevertheless, an RMS error of 135 m could be deemed as a preliminary error estimate.

4. Results

Mean H_{top} (*GOES-10*) from Eq. (2) and CF during the period of study are depicted in Fig. 4 (colors and contours, respectively). We note that while H_{top} was calculated only for $CF > 0.9$, CF maps were analyzed irrespective of the CF threshold. The general features are fairly consistent with Z09, with coastal shoaling of the boundary layer that yields H_{top} minima near 30°S (~ 700 m), but with larger heights at 20°S , 70°W (Arica bight, ~ 1200 m). The H_{top} zonal gradient, which peaks at about 1600 m over the westernmost point of the domain, is also in agreement with radiosonde observations (Brunke et al. 2010). Similar to other satellite climatologies (e.g., Wyant et al. 2010; Z09), CF is a maximum over the $15^\circ\text{--}23^\circ\text{S}$, $72^\circ\text{--}80^\circ\text{W}$ quadrant.

a. Diurnal evolution

The diurnal evolution in H_{top} and cloud fraction is illustrated in Figs. 5 and 6, respectively. These maps are subsets of hourly averaged retrievals for the study period. As expected, H_{top} and CF are high during the early morning with maxima around 0700 and 0400 LST, respectively. The afternoon reduction in cloud height and fraction reaches a minimum at 1600 LST, and there

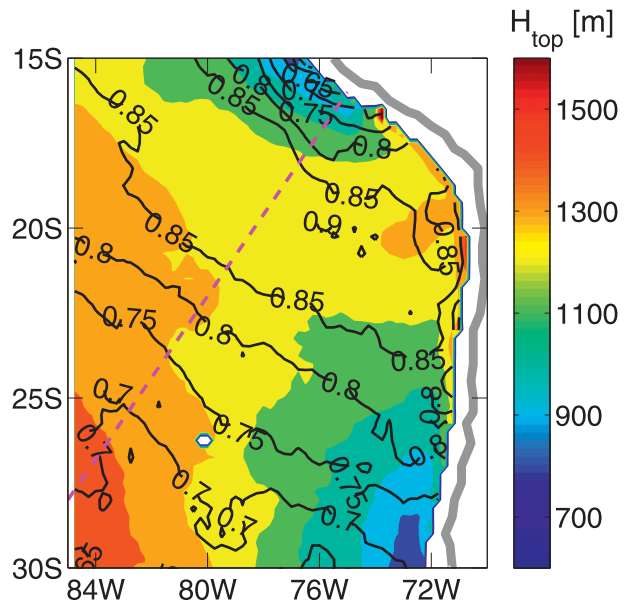


FIG. 4. Mean *GOES-10* H_{top} (colors) and CF (black contours) from *GOES-10* during the period of study. Magenta dashed line corresponds to the transect reported in Rahn and Garreaud (2010), which was used to construct Figs. 7 and 8.

is a recovery thereafter. The time when CF is smallest is consistent with the *GOES-10* liquid water path and cloud optical thickness minima described by Painemal et al. (2012). The afternoon reduction in CF and LWP is related to the solar heating. In addition, numerical and observational evidence (e.g., Medeiros et al. 2012; de Szoeke et al. 2012) also indicates that the midafternoon liquid water decrease is controlled by the coincident decoupling of the boundary layer. Another relevant feature is the rather dissimilar evolution of the coastal clouds relative to their far-offshore counterparts. In terms of H_{top} , the coastal clouds lead the afternoon deepening of the boundary layer. This is particularly evident over the Arica bight (20°S , 72°W), where positive anomalies occurred during 1900–2200 LST. These positive anomalies reveal a westward progression, with a detachment from the coast at 0100 LST, and with their westernmost location at 0400 LST. This coherent westward displacement is absent in CF (Fig. 6).

A closer examination of the southwestward-oriented hourly variability in H_{top} and CF, in the context of the subsidence forcing, is confined to the transect line in Fig. 4 (magenta dashed line). This transect was selected because it follows the propagation of the diurnal subsidence wave found in numerical simulations (Rahn and Garreaud 2010). The Hovmöller diagrams in Fig. 7 show the H_{top} , LWP, and CF anomalies (relative to the daily mean at each grid point) as functions of local time and the distance from the coast. The H_{top} and LWP

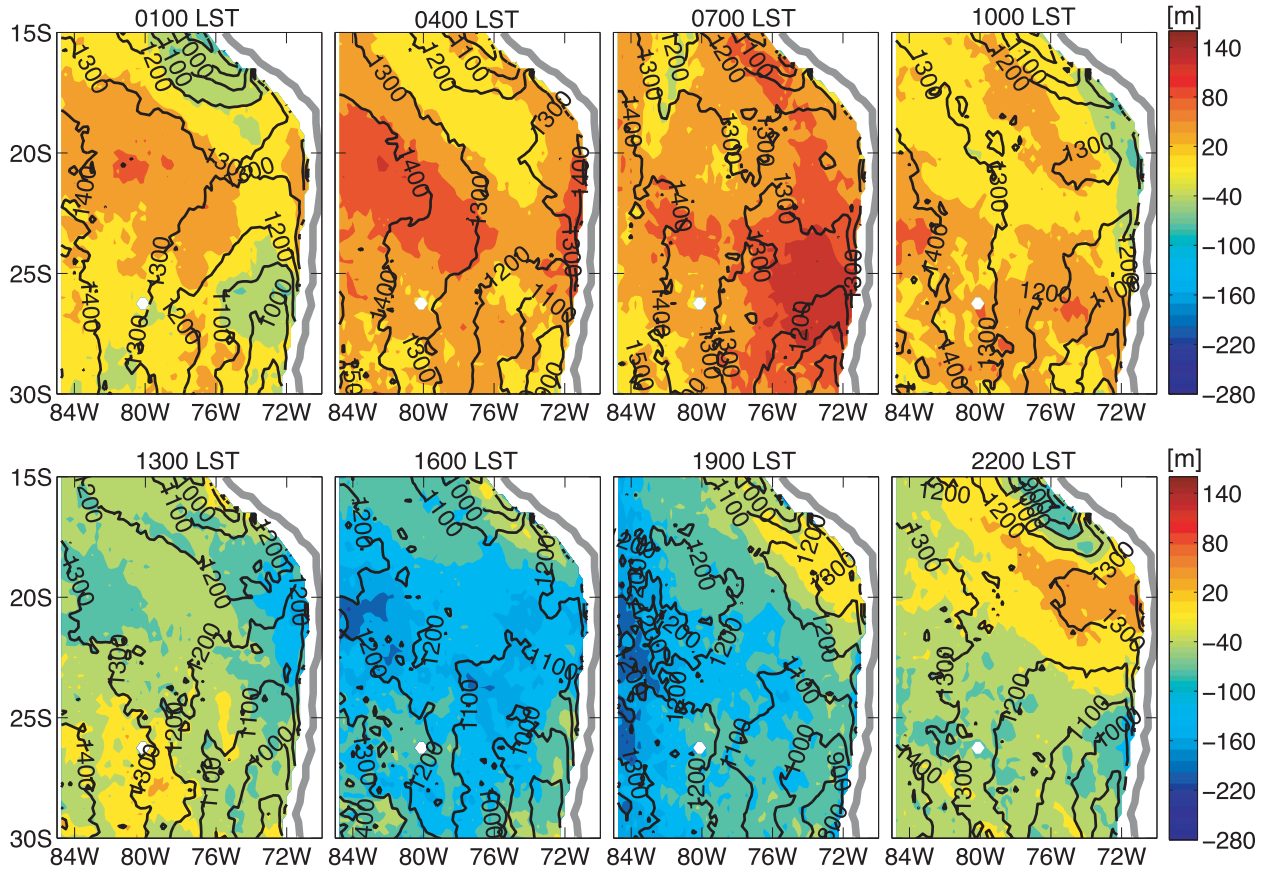


FIG. 5. Three-hourly mean H_{top} anomalies and mean values (colors and contours, respectively). LST calculated relative to 75°W.

anomalies (Fig. 7a, colors and black contours, respectively) indicate a salient westward propagation of positive values, with minima that occur around 1400–1700 LST, independent of the distance from the coast. As anticipated from the results in Fig. 6, a CF anomaly movement is not obvious (Fig. 7b), although a small westward propagating signal is suggested only a few hundred kilometers away from the coast (near zero contours in the 200–600-km and 1930–0130 LST quadrant in Fig. 7b).

For a better visualization of the southwestward-propagating H_{top} anomalies, we subtracted the single transect's cycle spatial average from the anomalies in Fig. 7. The results are plotted in Fig. 8a and overlaid with the satellite microwave LWP climatological departures calculated in the same manner as those for H_{top} (contours). To facilitate the discussion of the subsidence wave, we reproduced in Fig. 8b the vertical velocity anomalies at 2 km MSL along the same transect simulated by Rahn and Garreaud (2010, their Fig. 10). The westward propagation of H_{top} in Fig. 8a is evident, with an approximate speed of 23–25 m s^{-1} , and is in phase with the

LWP evolution (Fig. 8a, contours), suggesting a dual impact likely driven by the subsidence wave that propagates at speeds near 25 m s^{-1} in numerical simulations during VOCALS-REx (Toniazzo et al. 2011). This is more clearly depicted in Fig. 8b with anomalous positive vertical velocities that precede the positive H_{top} anomalies (solid black contours). The 3-h-temporal-resolution maps in Rahn and Garreaud (2010) prevent us from calculating the exact phase difference between vertical velocity and H_{top} , although the figure suggests phase differences of less than 3 h, consistent with Wood et al. (2009). The dynamical link between H_{top} , LWP, and subsidence will be further analyzed in sections 5 and 6. The corresponding Hovmöller diagram for CF departures (not shown) does not show a coherent propagating signal, in agreement with Fig. 7b.

b. Semidiurnal and diurnal cycle

To further investigate the rich spatial features in CF and H_{top} in terms of their diurnal and semidiurnal components, we fitted the following two-component harmonic to the 2-month mean hourly data:

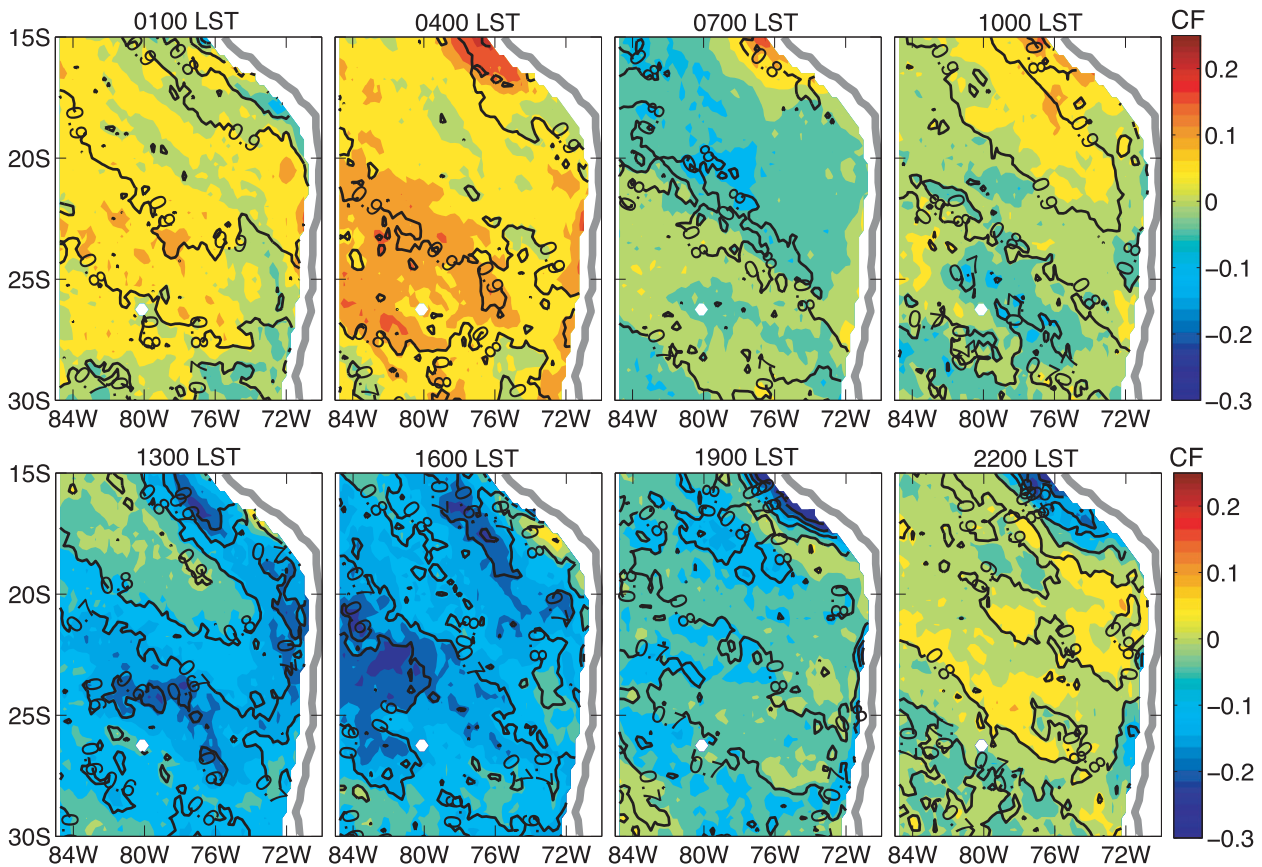


FIG. 6. As in Fig. 5, but for CF.

$$H_{\text{top}}(t) = \overline{H}_{\text{top}} + H_{\text{top12}} \cos \left[\frac{2\pi}{12}(t - \phi_{12}) \right] + H_{\text{top24}} \cos \left[\frac{2\pi}{24}(t - \phi_{24}) \right], \quad (3a)$$

$$\text{CF}(t) = \overline{\text{CF}} + \text{CF}_{12} \cos \left[\frac{2\pi}{12}(t - \phi_{\text{cf12}}) \right] + \text{CF}_{24} \cos \left[\frac{2\pi}{24}(t - \phi_{\text{cf24}}) \right]. \quad (3b)$$

The values $\overline{H}_{\text{top}}$ and $\overline{\text{CF}}$ correspond to the daily mean values, H_{top12} and CF_{12} and H_{top24} and CF_{24} represent the amplitudes of the semidiurnal and diurnal cycles, whereas the semidiurnal and diurnal phases are denoted by the pairs ϕ_{12} and ϕ_{cf12} and ϕ_{24} and ϕ_{cf24} , respectively. The constants in Eqs. (3a) and (3b) were calculated through a minimization of the sum of squared residuals, using a nonlinear optimization based on the Nelder–Mead method.

Figure 9 shows a coastal and a far-offshore example of the mean hourly H_{top} and CF with their corresponding sinusoidal fits from Eqs. (3). The coastal cloud deck has

two peaks in both H_{top} and CF near 0700 and 2300 LST (black lines and circles), whereas the offshore cloud cycle is mainly dominated by a 24-h cosine component, with broader amplitudes as well (Fig. 9, red circles).

The amplitude maps for the 12-h (H_{top12} and CF_{12}) and 24-h (H_{top24} and CF_{24}) harmonics are depicted in Fig. 10. In a close agreement with the LWP analysis of O'Dell et al. (2008), the H_{top} semidiurnal amplitude is a maximum at 22°S, 75°W, with amplitudes near 70 m (Fig. 10a). Similarly, the CF semidiurnal amplitude is a maximum over the same coastal region, with amplitudes around 6% ($\text{CF} \times 100$, Fig. 10a, contours). In contrast, the 24-h maximum amplitudes (Fig. 10b) are located far offshore (~ 130 m and 14% in CF at 23°S, 83°W), with minima over the region in which the semidiurnal harmonic is the largest (10–40 m, 8%). The 12-h to 24-h amplitude ratio (Fig. 10c) indicates that the H_{top} semidiurnal amplitude near the coast between 15° and 22°S is comparable to or slightly larger than its 24-h counterpart. For the coastal region south of 23°S, the H_{top} semidiurnal amplitude is only about $1/4$ the magnitude of the diurnal amplitude, whereas the semidiurnal amplitude drops to $1/8$ of the diurnal component over the westernmost

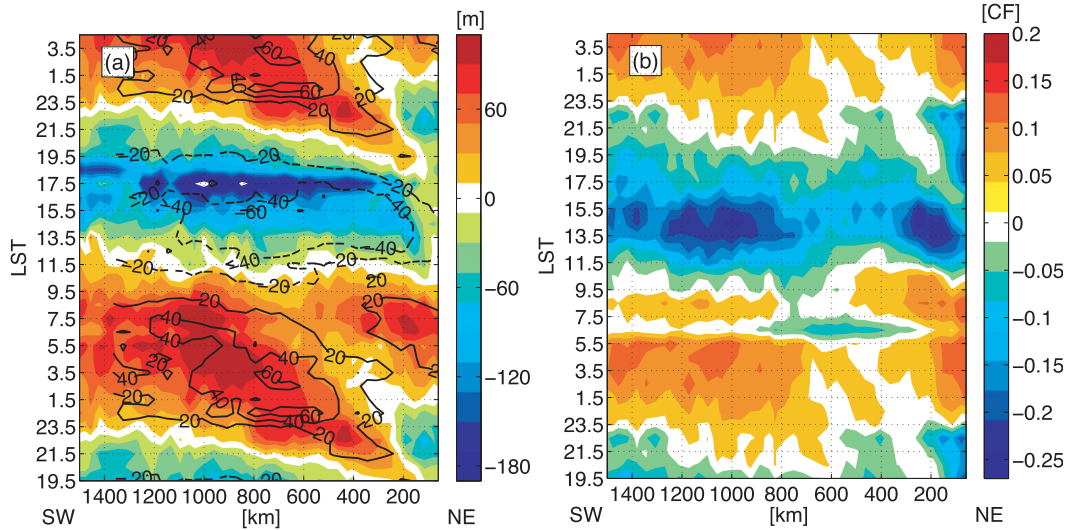


FIG. 7. Hovmöller diagram for anomalies along the transect in Fig. 4: (a) H_{top} and LWP (contours) and (b) CF. LST is calculated relative to 75°W (UTC - 5 h). For clarity, the diurnal cycle is repeated 5 h before and after the actual 24-h cycle.

point of the domain. While a qualitatively similar pattern for the CF 12-h to 24-h ratio is apparent (Fig. 10c, contours), the ratios are smaller than those for H_{top} .

The fraction of variance explained by each harmonic is depicted in Figs. 11a and 11b for H_{top} and CF, respectively. As expected, over the region having the largest H_{top} semidiurnal amplitude, the fractions of variance explained by each harmonic are similar, whereas for offshore regions, the diurnal harmonic explains more than 80% of the variance. South of 23°S, the littoral semidiurnal variance for H_{top} fluctuates between

0.1 and 0.25. The variance explained by the semidiurnal harmonic of CF is smaller than its H_{top} counterpart, with typical magnitudes fluctuating between 0.1 and 0.3.

5. Discussion

a. GOES-10 H_{top} and CF comparison to in situ observations

The satellite-based boundary layer height and cloud cover are remarkably similar to measurements collected

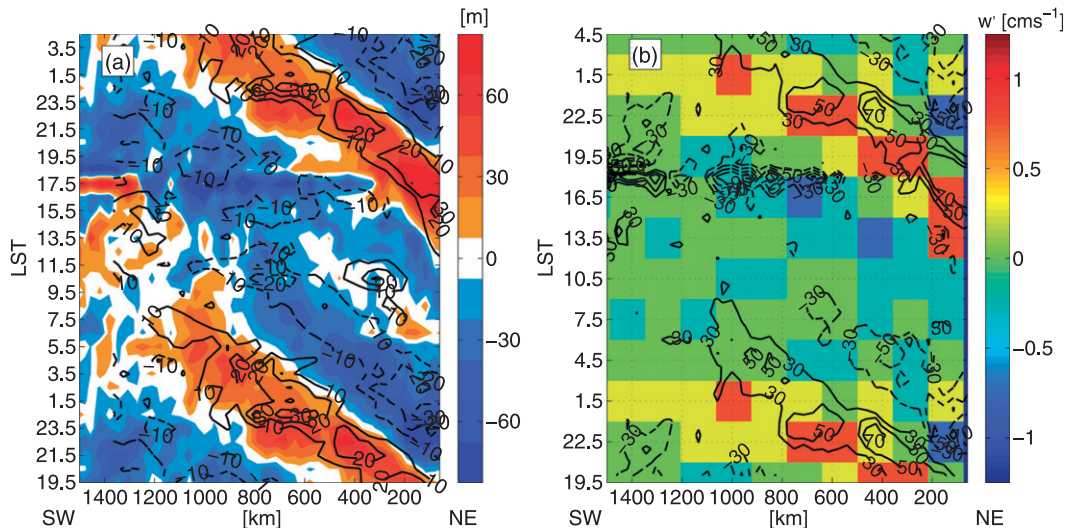


FIG. 8. (a) Hovmöller diagram for H_{top} (colors) and LWP ($g\ m^{-2}$; black contours) along the magenta line in Fig. 4. The values correspond to departures from the transect's spatially averaged diurnal cycle anomalies. (b) Vertical velocities anomalies at 2-km height every 3 h reported in Rahn and Garreaud (2010, their Fig. 10). For comparison purposes, H_{top} departures contours are also overlaid.

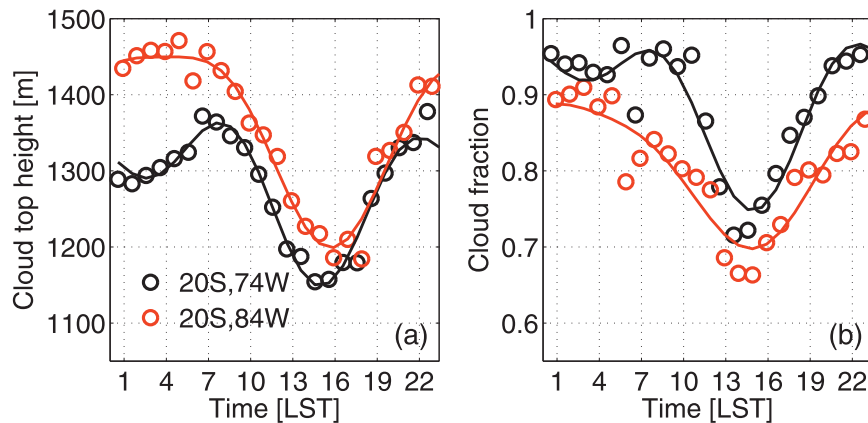


FIG. 9. Means (symbols) and associated harmonic fits (curves) for (a) H_{top} and (b) CF for a coastal (20°S , 74°W) and an offshore region (20°S , 84°W).

by the research vessel *Ronald Brown* along the 20°S parallel (de Szoeke et al. 2012). Ceilometer-based mean CF at 75° – 85°W yielded values between 0.64 and 0.95, with a minimum near 1500 LST. In addition, inversion base heights from radiosondes, over the same region, were approximately 1200–1500 m, with a minimum around 1400–1600 LST (Fig. 8 in de Szoeke et al. 2012). These values agree with the results in Fig. 9.

The zonal contrast in our retrievals is also in close agreement with radar observations during VOCALS-REx (Bretherton et al. 2010). Airborne radar observations along 20°S showed cloud-top-height medians around 1500 m at 85°W , whereas the cloud tops had

a relatively constant height near 1250 ($\sim 78^{\circ}\text{W}$) and 1200 m ($\sim 74^{\circ}\text{W}$) eastward. The mean map in Fig. 4 reveals a similar pattern, with mean cloud tops of 1380 m at 85°W , a relatively constant height to the east (1250–1200 m), but with a sudden height increase to 1300 m confined to the Arica bight (20°S , 72°W). Some differences at 85°W between the airborne radar and mean *GOES-10* H_{top} can be explained by the fact that most of the aircraft sampling over this region occurred early in the morning, when the H_{top} is at a maximum (early morning *GOES-10* H_{top} reaches up to 1500 m at 85°W). The H_{top} increase at Arica bight was also observed in Z09 and is closely associated with warmer sea surface

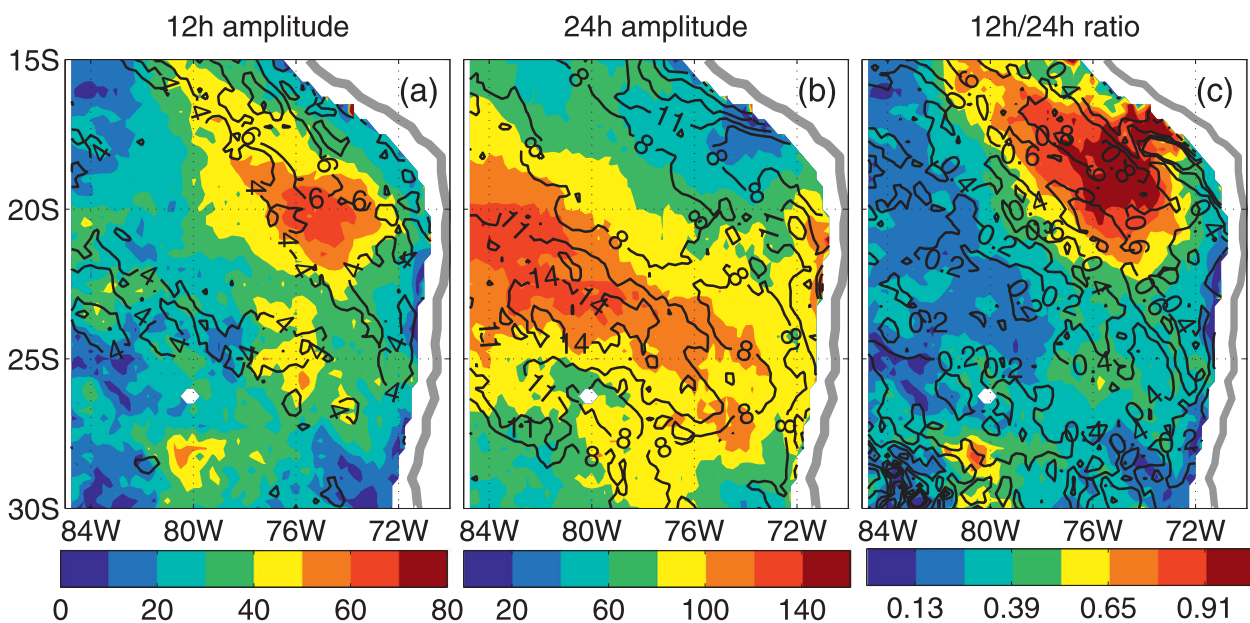


FIG. 10. (a) Amplitude of the 12-h harmonics for H_{top} (m; colors) and CF (%; CF $\times 100$; contours). (b) As in (a), but for the 24-h harmonics. (c) Ratio between the 12- and 24-h amplitudes for H_{top} (colors) and CF contours.

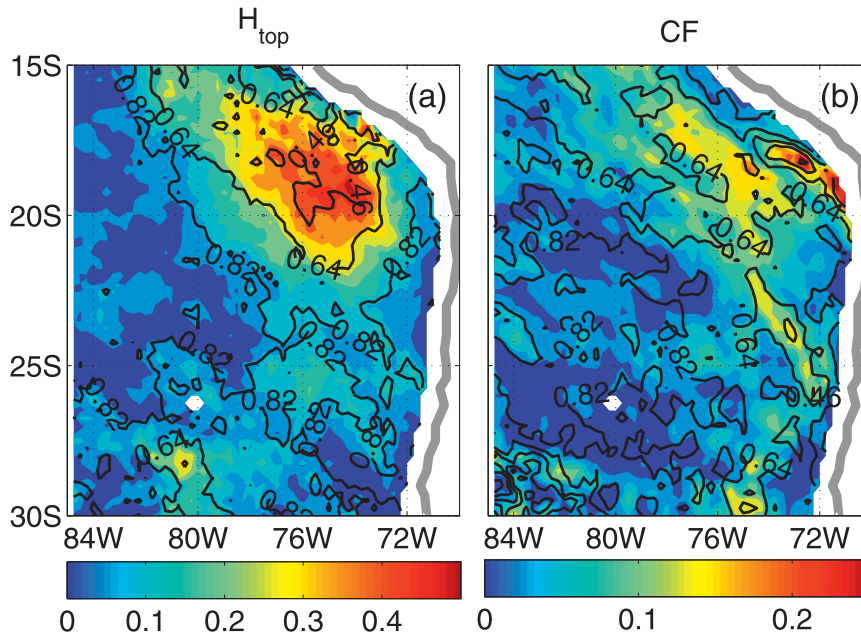


FIG. 11. Fraction of variance explained by the 12- (colors) and 24-h harmonics (contours): (a) H_{top} and (b) CF.

temperatures, which leads to greater cloud-top heights, particularly in late spring/early summer, and is possibly linked to a subsidence reduction (surface convergence) due to the mountain blocking effect. Twin Otter aircraft observations during VOCALS-REx near Arica bight (20°S , 72°W) sampled a mean boundary layer depth of $1150 \pm 120\text{ m}$ (Zheng et al. 2011), which is shallower than the *GOES-10* H_{top} mean. Part of this inconsistency has to do with the temporal sampling of the Twin Otter aircraft that mostly occurred between 0600 and 1400 local time, with only a few samples per day. We note that for this time window, *GOES-10* H_{top} typically encompasses values between 1200 and 1300 m. Thus, in situ observations suggest a slight overestimate of *GOES-10* H_{top} at Arica bight, but with mean values within the range of variability of the aircraft sampling.

The alongshore H_{top} gradient, with shallower clouds southward, qualitatively agrees with radiosonde observations at four land sites along the coast (Rahn and Garreaud 2010). Evidence of the meridional change in H_{top} was also found in the C-130 aircraft measurements used in section 3, with mean cloud tops at 1170 and 876 m along 20° – 22°S and 26° – 30°S , respectively, east of 74°W . Despite the coastal sampling limitation of the C-130, the aforementioned values are close to or slightly less than their mean *GOES-10* counterparts, with heights of 1275 (20° – 22°S) and 910 m (26° – 30°S).

The semidiurnal and diurnal harmonics for CF and H_{top} derived from *GOES-10* also agree with the ship observations when the *Ronald Brown* was stationed at

20°S , 75°W and at 20°S , 85°W during eight periods in austral spring from 2001 to 2008. Table 1 summarizes the fraction of the variance explained by the diurnal and semidiurnal CF and H_{top} harmonics from ship observations and the *GOES-10* retrievals. The in situ and *GOES-10* variances have similar magnitudes, with the larger variance explained by the semidiurnal cycle for the near-coastal H_{top} and CF, but with a smaller CF amplitude (≤ 0.27), as also found in Fig. 11. A similar spatial contrast in the semidiurnal CF amplitude was found for these same locations in November 1978 using *GOES-2* data (Minnis and Harrison 1984), indicating that the near-coastal semidiurnal cycle is a persistent climatological feature.

b. Subsidence and H_{top} cycle

Figure 12 shows the time for the occurrence of the second (afternoon–night) 12- and the 24-h maxima

TABLE 1. Fraction of variance explained by the semidiurnal and diurnal harmonics. In situ values are from de Szoeke et al. (2012).

	H_{top}		CF	
	In situ	<i>GOES-10</i>	In situ	<i>GOES-10</i>
Semidiurnal				
20°S , 75°W	0.48	0.40	0.21	0.27
20°S , 85°W	0.01	0.07	0.14	0.01
Diurnal				
20°S , 75°W	0.45	0.52	0.70	0.56
20°S , 85°W	0.90	0.89	0.79	0.82

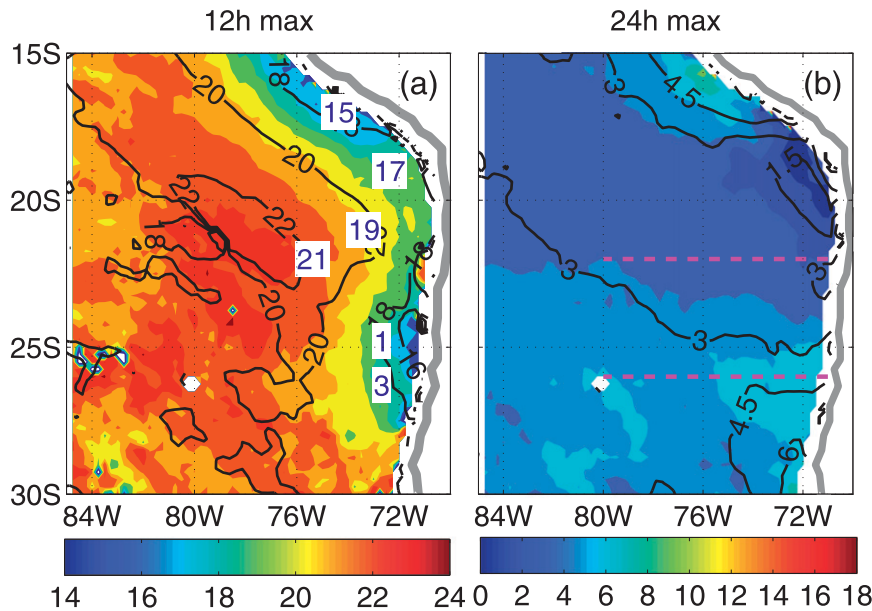


FIG. 12. (a) LST occurrence of the 12-h maximum (second maximum) for H_{top} (colors) and LWP (contours). Values in white background correspond to the approximate maximum occurrence of the upward velocity diagnosed by Gerreaud and Muñoz (2004). (b) As in (a), but for the 24-h maximum.

(phase) in H_{top} (colors) and LWP (contours). The semidiurnal and diurnal harmonics for LWP were calculated as in Eqs. (3). The second 12-h maximum (Fig. 12a) occurs first along the coastal strip at 1700–1800 LST, with a progressive delay to the west, until attaining a 2200–2300 LST phase at 22°S, 80°W. The 24-h maxima are mostly confined between 0100 and 0300 LST and are equivalent to a 24-h-cycle minimum around 1300–1500 LST. This 24-h afternoon minimum implies a destructive interference with the semidiurnal cycle for coastal clouds, whereas a constructive interference is more likely for offshore clouds (24-h-cycle anomalous amplitudes become positive after 1900–2100 LST). This pattern, consistent with the inversion temperature changes attributed to the subsidence cycle in Rahn and Garreaud (2010), is also followed by a similar evolution in liquid water path, over the region in which the semidiurnal harmonics are large (Fig. 12, contours).

The wavelike propagation pattern of the semidiurnal phase (Fig. 12a) closely resembles the modeled subsidence wave in Rahn and Garreaud (2010) and Garreaud and Muñoz (2004). To facilitate the physical interpretation of our results, we overlaid in Fig. 12a the approximate core location and time occurrence of the upward velocity fields diagnosed in Garreaud and Muñoz (2004) (numbers on white background) and summarized in their Fig. 5. The first maximum in the 12-h H_{top} harmonic, north of 17°S at 1700 LST, is spatially

consistent with the region in which the model diagnosed the origin of the vertical velocity perturbation, with positive anomalies approximately at 1500 LST, or 1.5–2 h prior to the H_{top} semidiurnal maximum. The detachment of the positive vertical velocity from the coast at 1900 LST also occurs in the 12-h harmonic but 2 h later (2000–2100 LST at 77°W). Similarly, a maximum upward motion at around 22°S, 75°W (2100 LST) has its semidiurnal H_{top} counterpart occurring around 2200–2300 LST.

The similarities between the H_{top} and LWP 12-h harmonics and the subsidence cycle can be tracked throughout the domain, except for a coastal region centered at 24–27°S. In this location, the semidiurnal maxima for H_{top} and LWP (Fig. 12a) occur almost 6 h before the anomalous positive vertical velocity wave reaches the southern coast (0100–0300 LST). This disparity suggests an additional forcing acting in concert near 25°S, an idea that is further supported by numerical evidence (Muñoz 2008). Over this region, along with the aforementioned propagating wave, Muñoz (2008) observes a zonally propagating positive vertical velocity pulse near 1500 LST and below 1000 m that extends up to 3° westward. This anomaly co-occurs with an eastward surface wind pattern in connection with the land–sea breeze circulation. Muñoz (2008) hypothesizes that a surface convergence/divergence pattern associated with afternoon eastward winds and the plausible effect

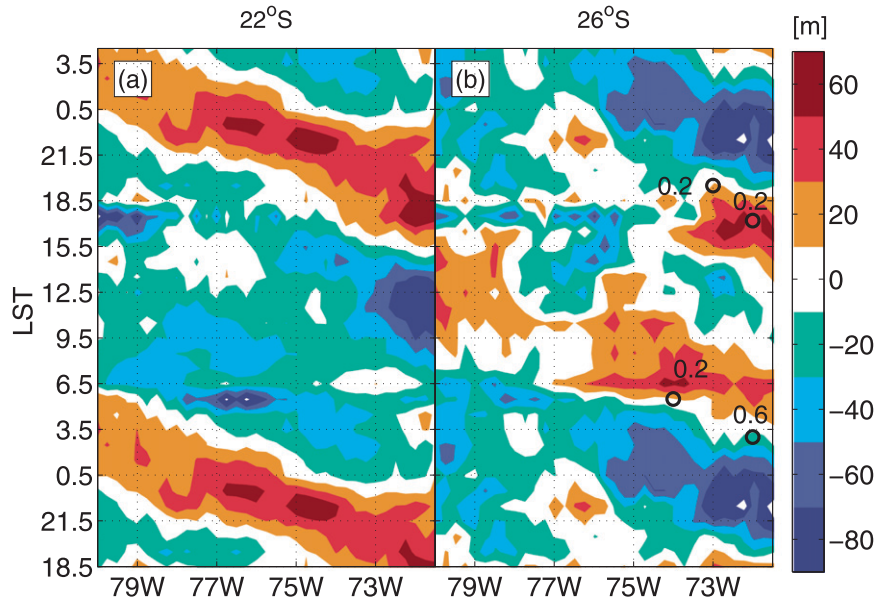


FIG. 13. Hovmöller diagrams for two westward transects of H_{top} departures fixed at (a) 22° and (b) 26° S. Departures were calculated relative to a common standard diurnal cycle, which was in turn computed as the composited zonally averaged cycle from both transects. Black circles and numbers correspond to the approximate location and maximum values of the anomalous updraft below 1000 m diagnosed in Muñoz (2008).

of the topography could explain the origin of the coastal upward motion at 26° S (Muñoz 2008). We evaluate our results in the context of Muñoz (2008) by comparing the westward/temporal variation of the cloud-top-height signal at 22° and 26° S (transects denoted by the magenta dashed lines in Fig. 12b). As in Fig. 8a, the anomalous diurnal cycles at each grid point were subtracted by a common standard diurnal cycle. This cycle was estimated as the single composited and zonally averaged anomalous diurnal cycle from the two zonal transects (Fig. 13). The Hovmöller diagram at 22° S (Fig. 13a) nicely depicts the dominant westward-propagating feature attributed to the subsidence wave, which reaches this coastal point around 1700–1900 LST, in agreement with the semidiurnal phase in Fig. 12a (1900–2000 LST). Four degrees south, at 26° S, the cloud-height spatial-temporal structure is more complex, with two main positive propagating signals (Fig. 13b). The morning pattern at 0530 LST is the response of the subsidence wave, which peaks at this location near 0300 LST (numbers in Fig. 13b, with axes denoted by black circles; from Muñoz 2008). A second propagating but short-lived feature near 1700 LST, with positive anomalies extending only 4° westward, explains the semidiurnal phase along 24° – 27° S in Fig. 12a. This pattern occurs almost simultaneously with a maximum in upward motion below 1 km reported in Muñoz (2008) and repeated in Fig. 13b. The qualitative agreement between the

semidiurnal phase H_{top} and the simulated vertical velocity is remarkable (numbers in Fig. 13b) and corroborates the idea that H_{top} increases are the consequence of positive vertical velocities within the boundary layer. We note that the simulations in Muñoz (2008) were performed for the December 2003 period, and therefore a slight disagreement in phase between H_{top} and vertical velocity should be expected.

Although this analysis covered a period in which the marine stratocumulus clouds had their maximum development, some seasonal features can be anticipated. With respect to the modulation of the subsidence wave, given the importance of the Andes heating in its genesis, we expect a reduction in the subsidence amplitude toward austral winter (Garreaud and Muñoz 2004). This should yield a smaller amplitude of the semidiurnal cycle in H_{top} as well. Evidence of this was reported by O'Dell et al. (2008) but for LWP in autumn. A reduction of the afternoon radiative heating during autumn and winter would also produce smaller amplitudes in the 24-h cycle of boundary layer depth. The determination of the exact seasonal dependence of the magnitudes of the H_{top} diurnal cycle will require extending this work with the use of a GOES dataset that can resolve the cloud seasonality.

This study along with a preceding paper on the daytime cycle of *GOES-10* cloud microphysics (Painemal et al. 2012) provides a holistic satellite view of the

stratocumulus diurnal cycle over the southeastern Pacific domain. In addition to the assessment of *GOES-10* retrievals presented here and in Painemal et al. (2012), the influence of a strong afternoon forcing was evident in both LWP and cloud effective radius. A rapid coastally confined increase in cloud optical thickness τ and cloud effective radius r_e at 1600 LT is consistent with a decrease in subsidence (and sometimes upward motion) associated with the subsidence wave. Moreover, increases of coastal r_e and τ south of the region where the subsidence wave is dominant suggest the dynamical influence of the land–sea breeze, with afternoon eastward winds that would induce positive vertical velocities, as observed by Muñoz (2008) and discussed previously. From a cloud–aerosol interaction perspective, this is also relevant, as reduced aerosol concentrations, due to air advected from more pristine oceanic regions during the afternoon, would also contribute to larger r_e . Although the time occurrence of the minimum in H_{top} and τ (LWP) are nearly identical, with a progressive zonal delay to the west, r_e yields a mostly constant phase with minima around 1230–1300 LST. This might point to the dominant sensitivity of r_e to the solar radiative heating during the early afternoon. The contribution of each forcing in the r_e evolution will require further investigation and modeling efforts.

6. Summary

We used *GOES-10* retrievals to investigate the diurnal cycle in cloud-top height and cloud fraction over the southeastern Pacific during October–November 2008. Because H_{top} calculations are a function of the *GOES-10* cloud-top temperature, we first compared *GOES-10* against MODIS and in situ T_{top} . Excellent agreement and negligible biases between *GOES-10* T_{top} and those from MODIS (*Terra* and *Aqua*) cloud-top temperatures demonstrate the good *GOES-10* 10.7- μm channel calibration. Nevertheless, a negative bias of *GOES-10* cloud-top temperature relative to its in situ counterpart corroborated the presence of a negative offset in satellite retrievals that was also found in Z09 but for MODIS. While this satellite bias has not been thoroughly explained, it is likely due to differences in the cloud-top droplet and ambient air temperatures.

The high linear correlation between the sea surface–cloud-top temperature difference and the in situ cloud-top height justified the use of a simple linear relationship to estimate H_{top} from T_{top} (*GOES-10*). We applied the linear regression to matched T_{top} (*GOES-10*) and SST_{TMI} data and found that the satellite and in situ H_{top} values agree well, having a negligible bias and a linear correlation coefficient of 0.85. From a remote sensing

perspective, a result of interest is the cold *GOES-10* T_{top} bias relative to the aircraft observations. This finding is robust as an independent study (Z09) that used different in situ and satellite observations, and with a different retrieving algorithm, arrived to similar conclusions. We believe that cloud droplets colder than the ambient air, due to evaporation (entrainment) and longwave cooling, could affect the satellite retrievals since the sensors primarily measure emission from the clouds. If this hypothesis is correct, then one should expect to observe a similar T_{top} trait in other boundary layer clouds. Unfortunately, satellite T_{top} and in situ comparisons in other regions are scarce. Nevertheless, systematic cold CERES T_{top} biases in continental stratus clouds over the southern Great Plains (36°S, 97°W; Dong et al. 2008) and in marine stratocumulus clouds over Graciosa Island (39°N, 28°W; Xi et al. 2012) partially confirm our expectation.

Our retrievals reproduced the main features of the marine stratocumulus observed in the Z09 climatology and agreed with independent in situ observations over the region of study. In situ and satellite retrievals consistently show higher cloud tops relative to those found off the western coast of California (e.g., Stevens et al. 2003; Z09). In terms of the diurnal cycle, increases in H_{top} and CF during the early morning give witness to a deepening cloudy boundary layer and are followed by decreases, reaching minimum magnitudes during the afternoon. Diurnal cycle spatial differences are also evident, with coastal clouds producing a more complex cycle than their offshore counterparts, manifested in a semidiurnal cycle in both H_{top} and CF. The strongest semidiurnal signal was found at 18°S, 75°W, with an amplitude of about 80 m and an explained fraction of variance (≤ 0.5) for H_{top} that are similar to those associated with the 24-h-cycle values. In contrast, the semidiurnal cycle in CF is less conspicuous, and the fraction of explained variance is typically smaller as well (≤ 0.3). This indicates that CF is less sensitive to the impact of the subsidence wave, primarily because CF in the late afternoon and night is high, whereas LWP can still have large variability. The location and the strength of the H_{top} semidiurnal cycle are in close agreement with satellite-microwave liquid water path climatologies (e.g., O’Dell et al. 2008) and reveal a westward propagation in phase as well. The second maximum of the H_{top} semidiurnal harmonic shows a consistent earlier maximum along the coast, with a temporal–spatial evolution correlated with the simulated subsidence wave and with an apparent delay of 2–3 h. Our findings also reveal the modulation of an additional ascending motion pattern confined along the 24°–28°S coast, associated with the eastward winds from the

land–sea breeze circulation and plausible local topographical effects (Muñoz 2008).

The similarity of the evolution and westward propagation of *GOES-10* H_{top} and LWP anomalies to subsidence anomalies predicted in numerical modeling studies strongly suggests that the former is a response to the latter. The control of subsidence on H_{top} has a straightforward interpretation in a mixed-layer model framework. Temporal variations of the boundary layer height h are the direct contribution of the large-scale subsidence w_s and entrainment rate w_e , or $dh/dt = w_s + w_e$. It follows that a reduction in subsidence will result in an anomalous increase of the boundary layer depth (and H_{top}). Moreover, adiabatically cooler air temperatures above the inversion, due to reductions in subsidence, will decrease the temperature-inversion jump, and therefore, it will yield stronger entrainment and deeper heights. The link between subsidence, entrainment and LWP is more difficult to interpret. The expected drying of the boundary layer due to entrainment has to necessarily be balanced by other factors in order to produce the observed LWP increase. Since the subsidence wave propagates from the coast after 1500 UTC, the progressive afternoon decrease in the solar radiative heating allows the cloud-top longwave radiative cooling to build up turbulence and overcome the midafternoon decoupling. This midafternoon decoupling occurs with a maximum in the specific humidity because of surface evaporation, and it might supply the necessary moisture for the progressive LWP recovery later on (de Szoek et al. 2012). Strong turbulence generation and a more coupled boundary layer would be able to produce enough condensation (in connection with strong moisture fluxes) to account for an LWP increase when the boundary layer height deepens, after the late afternoon passage of the subsidence wave. This would also enable r_e to increase, as observed in Painemal et al. (2012). What seems clear is that the moisture transport must be sufficient to overcome evaporation due to entrainment under well-mixed conditions.

The unprecedented spatial and temporal resolutions of our analysis have provided a spatial context to in situ observations and have helped explain features that are not easily reproduced in numerical models. This analysis was confined to a particular region and used only 2 months of data. Although we expect that the results are representative of this area, similar analyses using more temporally extensive data would be valuable to determine the seasonal variability of the interactions between the diurnal subsidence waves and the cloud properties. Additionally, analyses of data taken over other marine stratocumulus regions would be necessary to determine if and how the

subsidence fields affect marine stratocumulus near other coastlines.

Acknowledgments. D. Painemal is supported by the NASA Postdoctoral Program at NASA Langley Research Center, administered by Oak Ridge Associated Universities (ORAU). P. Minnis is supported by the NASA Modeling, Analysis, and Prediction and CERES Programs and by the U.S. Department of Energy's Atmospheric Science Program Atmospheric System Research Interagency Agreement DE-SC0000991/003. L. O'Neill is supported by Grant NNX11AF31G through NASA's Ocean Vector Winds Science Team and an institutional fellowship through Oregon State University. The comments and suggestions of three anonymous reviewers are greatly acknowledged.

REFERENCES

- Abel, S. J., D. N. Walters, and G. Allen, 2010: Evaluation of stratocumulus cloud prediction in the Met Office forecast model during VOCALS-REx. *Atmos. Chem. Phys.*, **10**, 10541–10559, doi:10.5194/acp-10-10541-2010.
- Allen, G., G. Vaughan, T. Tonlazzo, H. Coe, P. Connolly, S. Yuter, C. Burleyson, P. Minnis, and J. K. Ayers, 2012: Gravity wave-induced perturbations in marine stratocumulus. *Quart. J. Roy. Meteor. Soc.*, **138**, 1970–1982, doi:10.1002/qj.1947.
- Bretherton, C. S., R. Wood, R. C. George, D. Leon, G. Allen, and X. Zheng, 2010: Southeast Pacific stratocumulus clouds, precipitation and boundary layer structure sampled along 20°S during VOCALS-REx. *Atmos. Chem. Phys.*, **10**, 10639–10654, doi:10.5194/acp-10-10639-2010.
- Brunke, M. A., S. P. de Szoek, P. Zuidema, and X. Zeng, 2010: A comparison of ship and satellite measurements of cloud properties with global climate model simulations in the southeast Pacific stratus deck. *Atmos. Chem. Phys.*, **10**, 6527–6536, doi:10.5194/acp-10-6527-2010.
- Caldwell, P., and C. S. Bretherton, 2009: Large-eddy simulation of the diurnal cycle in southeast Pacific stratocumulus. *J. Atmos. Sci.*, **66**, 432–449.
- de Szoek, S., S. Yuter, D. Mechem, C. W. Fairall, C. Burleyson, and P. Zuidema, 2012: Observations of stratocumulus clouds and their effect on the eastern Pacific surface heat budget along 20°S. *J. Climate*, **25**, 8542–8567.
- Dong, X., P. Minnis, B. Xi, S. Sun-Mack, and Y. Chen, 2008: Comparison of CERES-MODIS stratus cloud properties with ground-based measurements at the DOE ARM Southern Great Plains site. *J. Geophys. Res.*, **113**, D03204, doi:10.1029/2007JD008438.
- Garay, M. J., S. P. de Szoek, and C. M. Moroney, 2008: Comparison of marine stratocumulus cloud top heights in the southeastern Pacific retrieved from satellites with coincident ship-based observations. *J. Geophys. Res.*, **113**, D18204, doi:10.1029/2008JD009975.
- Garreaud, R. D., and R. Muñoz, 2004: The diurnal cycle of circulation and cloudiness over the subtropical southeast Pacific: A modeling study. *J. Climate*, **17**, 1699–1710.
- , J. Rutllant, J. Quintana, J. Carrasco, and P. Minnis, 2001: CIMAR-5: A snapshot of the lower troposphere over the subtropical southeast Pacific. *Bull. Amer. Meteor. Soc.*, **82**, 2193–2208.

- Gentemann, C. L., F. J. Wentz, C. A. Mears, and D. K. Smith, 2004: In situ validation of Tropical Rainfall Measuring Mission microwave sea surface temperatures. *J. Geophys. Res.*, **109**, C04021, doi:10.1029/2003JC002092.
- Holz, R. E., S. A. Ackerman, F. W. Nagle, R. Frey, S. Dutcher, R. E. Kuehn, M. A. Vaughan, and B. Baum, 2008: Global Moderate Resolution Imaging Spectrometer (MODIS) cloud detection and height evaluation using CALIOP. *J. Geophys. Res.*, **113**, D00A19, doi:10.1029/2008JD009837.
- Kawai, Y., and A. Wada, 2007: Diurnal sea surface temperature variation and its impact on the atmosphere and ocean: A review. *J. Oceanogr.*, **63**, 721–744.
- Medeiros, B., D. L. Williamson, C. Hannay, and J. G. Olson, 2012: Southeast Pacific stratocumulus in the Community Atmosphere Model. *J. Climate*, **25**, 6175–6192.
- Menzel, P., and Coauthors, 2008: MODIS global cloud-top pressure and amount estimation: Algorithm description and results. *J. Appl. Meteor. Climatol.*, **47**, 1175–1198.
- Minnis, P., and E. F. Harrison, 1984: Diurnal variability of regional cloud and clear-sky radiative parameters derived from GOES data, Part II: November 1978 cloud distributions. *J. Climate Appl. Meteor.*, **23**, 1012–1031.
- , P. W. Heck, D. F. Young, C. W. Fairall, and J. B. Snider, 1992: Stratocumulus cloud properties derived from simultaneous satellite and island-based instrumentation during FIRE. *J. Appl. Meteor.*, **31**, 317–339.
- , D. P. Garber, D. F. Young, R. F. Arduini, and Y. Takano, 1998: Parameterizations of reflectance and effective emittance for satellite remote sensing of cloud properties. *J. Atmos. Sci.*, **55**, 3313–3339.
- , and Coauthors, 2008: Cloud detection in non-polar regions for CERES using TRMM VIRS and Terra and Aqua MODIS data. *IEEE Trans. Geosci. Remote Sens.*, **46**, 3857–3884.
- , and Coauthors, 2011: CERES edition-2 cloud property retrievals using TRMM VIRS and Terra and Aqua MODIS data—Part I: Algorithms. *IEEE Trans. Geosci. Remote Sens.*, **49**, 4374–4400, doi:10.1109/TGRS.2011.2144601.
- Muñoz, R., 2008: Diurnal cycle of surface winds over the subtropical southeast Pacific. *J. Geophys. Res.*, **113**, D13107, doi:10.1029/2008JD009957.
- O'Dell, C. W., F. J. Wentz, and R. Bennartz, 2008: Cloud liquid water path from satellite-based passive microwave observations: A new climatology over the global oceans. *J. Climate*, **21**, 1721–1739.
- O'Neill, L. W., S. Wang, and Q. Jiang, 2011: Satellite climatology of cloud liquid water path over the southeast Pacific between 2002 and 2009. *Atmos. Chem. Phys. Discuss.*, **11**, 31159–31206, doi:10.5194/acpd-11-31159-2011.
- Painemal, D., and P. Zuidema, 2011: Assessment of MODIS cloud effective radius and optical thickness retrievals over the southeast Pacific with VOCALS-REx in situ measurements. *J. Geophys. Res.*, **116**, D24206, doi:10.1029/2011JD016155.
- , and P. Minnis, 2012: On the dependence of albedo on cloud microphysics over marine stratocumulus clouds regimes determined from Clouds and the Earth's Radiant Energy System (CERES) data. *J. Geophys. Res.*, **117**, D06203, doi:10.1029/2011JD017120.
- , —, K. Ayers, and L. O'Neill, 2012: GOES-10 microphysical retrievals in marine warm clouds: Multi-instrument validation and daytime cycle over the southeast Pacific. *J. Geophys. Res.*, **117**, D19212, doi:10.1029/2012JD017822.
- Rahn, D. A., and R. Garreaud, 2010: Marine boundary layer over the subtropical southeast Pacific during VOCALS-REx—Part 1: Mean structure and diurnal cycle. *Atmos. Chem. Phys.*, **10**, 4491–4506, doi:10.5194/acp-10-4491-2010.
- Richter, I., and C. R. Mechoso, 2006: Orographic influences on subtropical stratocumulus. *J. Atmos. Sci.*, **63**, 2585–2601.
- Stevens, B., and Coauthors, 2003: Dynamics and Chemistry of Marine Stratocumulus—DYCOMS-II. *Bull. Amer. Meteor. Soc.*, **84**, 579–593, doi:10.1175/BAMS-84-5-579.
- Toniazzo, T., S. J. Abel, R. Wood, C. R. Mechoso, G. Allen, and L. C. Shaffrey, 2011: Large-scale and synoptic meteorology in the south-east Pacific during the observations campaign VOCALS-REx in austral Spring 2008. *Atmos. Chem. Phys.*, **11**, 4977–5009, doi:10.5194/acp-11-4977-2011.
- Wentz, F. J., 1997: A well-calibrated ocean algorithm for Special Sensor Microwave/Imager. *J. Geophys. Res.*, **102**, 8703–8718.
- , and T. Meissner, 2000: AMSR ocean algorithm. Algorithm Theoretical Basis Doc. 121599A-1, Remote Sensing Systems, Santa Rosa, CA, 74 pp. [Available online at <http://eosppo.gsfc.nasa.gov/sites/default/files/atbd/atbd-amsp-ocean.pdf>.]
- , C. L. Gentemann, D. K. Smith, and D. B. Chelton, 2000: Satellite measurements of sea-surface temperature through clouds. *Science*, **288**, 847–850.
- Wood, R., 2012: Stratocumulus clouds. *Mon. Wea. Rev.*, **140**, 2373–2423.
- , M. Kohler, R. Bennartz, and C. O'Dell, 2009: The diurnal cycle of surface divergence over the global oceans. *Quart. J. Roy. Meteor. Soc.*, **135**, 1484–1493.
- , and Coauthors, 2011: The VAMOS Ocean-Cloud-Atmosphere-Land Study Regional Experiment (VOCALS-REx): Goals, platforms, and field operations. *Atmos. Chem. Phys.*, **11**, 627–654, doi:10.5194/acp-11-627-2011.
- Wyant, M. C., and Coauthors, 2010: The PreVOCA experiment: Modeling the lower troposphere in the southeast Pacific. *Atmos. Chem. Phys.*, **10**, 4757–4774, doi:10.5194/acp-10-4757-2010.
- Xi, B., X. Dong, S. Sun-Mack, P. Minnis, and Y. Chen, 2012: Validation of satellite retrieved marine low-level cloud properties using ARM AZORES results. *Proc. 18th CERES-II Science Team Meeting*, Princeton, NJ, NASA/GFDL, 33 pp. [Available online at http://ceres.larc.nasa.gov/documents/STM/2012-10/Thu_16_Baike.CERES.STM.10.12.pdf.]
- Xie, F., D. L. Wu, C. O. Ao, A. J. Mannucci, and E. R. Kursinski, 2012: Advances and limitations of atmospheric boundary layer observations with GPS occultation over southeast Pacific Ocean. *Atmos. Chem. Phys.*, **12**, 903–918, doi:10.5194/acp-12-903-2012.
- Xu, H., Y. Wang, and S. Xie, 2004: Effects of the Andes on eastern Pacific climate: A regional atmospheric model study. *J. Climate*, **17**, 589–602.
- Zheng, X., and Coauthors, 2011: Observations of the boundary layer, cloud, and aerosol variability in the southeast Pacific near-coastal marine stratocumulus during VOCALS-REx. *Atmos. Chem. Phys.*, **11**, 9943–9959, doi:10.5194/acp-11-9943-2011.
- Zuidema, P., D. Painemal, S. de Szoek, and C. Fairall, 2009: Stratocumulus cloud top estimates and their climatic implications. *J. Climate*, **22**, 4652–4666.